Development and a Limited Validation of a Whole-Body Finite Element Pedestrian and Occupant Models of a 10-Year-Old Child

Ming Shen[1], Feng Zhu, Binhui Jiang, Vikas Sanghavi, Haonan Fan, Yun Cai, Zhenguang Wang, Anil Kalra, Xin Jin, Clifford C. Chou, King H. Yang

Abstract Children aged around 10 years old (10 YO) are not as well protected as those below 6YO or adults in traffic accidents. To improve the protective means for occupant and pedestrian in this age group, it is imperative to enhance the research techniques. To overcome the limitations of testing post-mortem human subject (PMHS) or crash dummy, a whole-body pediatric finite element (FE) model (named CHARM-10) with anatomic details and reasonable biofidelity was developed. The model development and validation at component/body part level have been reported elsewhere and are briefly summarized in this paper. In this study, the integration of three main body regions (head-neck, thorax-upper extremities and pelvis-lower extremities) are described in detail. CHARM-10 has two postures (standing and seated) to represent a pediatric pedestrian and seated occupant, respectively. The standing posture model was used to corroborate the kinematic responses in car-to-pedestrian impact by comparing kinematics with a newly scaled 10 YO multi-body model. The seated posture model was validated against low-speed volunteer sled tests and a high-speed PMHS sled test data. In both pedestrian and occupant impact scenarios, reasonable agreements were obtained. The CHARM-10 models were therefore preliminarily validated but require further improvement before applications in automotive safety research.

Keywords finite element method, occupant impact, pedestrian impact, pediatric human model, traffic injury

I. INTRODUCTION

Road traffic related injuries and fatalities constitute a major daily public safety threat to children all over the world. In United Sates, it is the leading cause of death and disability for children based on data reported by Centers for Disease Control and Prevention (CDC) in 2010 [1]. Worldwide, traffic accident is also a top risk to children aged 4-15, in which about one-third of the deaths are to pedestrians, while two-thirds are to vehicle occupants [2]. Traffic injuries of children around 10 (8-12) years old (YO) should be paid particular attention, according to a review by Wazana et al. (1997) [3]. In 2012, the age group 8-14 accounted for the largest number of pedestrian fatalities among all ages of children [4]. In terms of occupant safety, motor vehicle restraint systems are not specifically designed for children around 10 YO. Most child occupants in this age group are transiting from using boosters to barely fitting in to seat belts, which are optimized for adult occupants. Additionally, they usually do not benefit from airbag when sitting in the rear rows and are even harmed by airbag when seated in the front seats [1].

In terms of pedestrian safety, the age group with the peak injury risk is between 6 and 10 years, as reported by NHTSA in: (1) Pedestrian injury Causation Study (PICS, 1977 to 1980) and (2) Pedestrian Crash Data Study (PCDS, 1955 to 1998) [5]. The pedestrian fatalities of age group 8-14 years accounted for more than the summation of the other child age groups [6]. Therefore, more in-depth studies on both pedestrian and occupant safety of children aged 8-12 years are demanded in order to better understand the injury mechanisms during impact accidents and to improve safety countermeasures.

Ming Shen is a PhD student in Bioengineering Center of Wayne State University, Detroit, US. (The corresponding author is King H. Yang, Prof. Phone: +1(313)577-0252, Email: aa0007@wayne.edu.) All authors are from this department, except Jiang from Hunan University, Changsha, China. Chou is Prof. Zhu and Jin are Assistant Prof. Jiang is post-doc fellow. Kalra is a PhD student and others are M.S. students at the time of the study.

Conventional methodologies employed in the traffic injury studies include post-mortem human subject (PMHS) tests, anthropometric test devices (ATDs) tests and computational simulations. Due to ethical considerations, it is extremely difficult to conduct a large number of pediatric PMHS tests. Consequently, data are rare and scattered. ATDs, such as Hybrid III crash dummies, are made from artificial and simplified structures, such as metallic tubes for long bones and rubber jacket for torso flesh. Therefore, the biofidelity of the ATDs need much improvement if injury mechanisms and tolerances are to be investigated in detail. Computational simulations usually include multi-body modeling and finite element (FE) modeling. Multi-body modeling is suited for straightforward kinematic and dynamic analysis, but also suffers from the over-simplification. To eliminate the aforementioned limitations, FE modeling has been widely accepted as a major alternative approach to supplement these tests and simulations. Some researchers have developed whole-body FE models for younger children [7, 8], while other researchers have created FE models for a number of body parts for children around 10 YO [9, 10]. However, to date, a full body FE model representing children around 10 YO is still missing. The most common whole-body FE model families of Total Human Model for Safety (THUMS) and Global Human Body Models Consortium (GHBMC) do not include a 10 YO model.

In this study, a 10 YO whole-body pediatric FE model with sufficient anatomic details has been developed at Wayne State University (WSU). This 10 YO pediatric FE model was developed in collaboration with Toyota Collaborative Safety Research Center (CSRC) and named Collaborative Human Advanced Research Models – 10 Years Old (CHARM-10).The development and validation work of the major body regions were completed and documented in the literature [11-15]. In this study, integration and preliminary validations of the whole-body model are emphasized.

II. MODEL DEVELOPMENT METHODS

Geometric data and mesh generation

The model development procedure included two main steps: (1) computer aided design (CAD) modeling and (2) meshing, as shown in Fig. 1. It is summarized as follows.

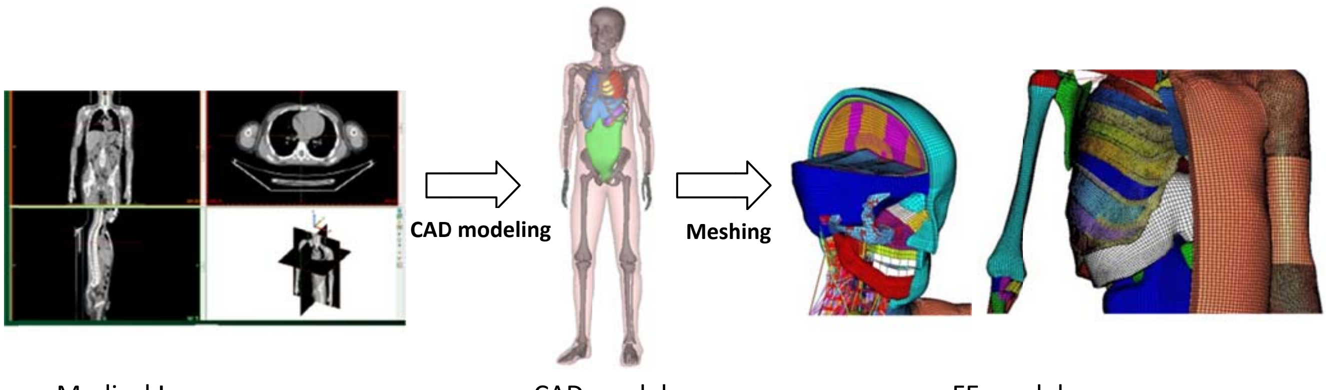

Fig. 1: Development procedures of the CHARM-10. Medical images includes computed tomography (CT) and magnetic resonance imaging (MRI) scans

For establishing high-quality geometric references, two phases of effort were made. In Phase One, clinical images from two subjects (one for CT and one for MRI) per body region were used to create an initial dataset of the geometry. The image data were collected from the Children's Hospital of Michigan, involving 12 children from 9.5-10.5 YO. An Institutional Review Board at Wayne State University approved the use of these images with all personal identities removed. The geometry was then scaled to an average-size 10 YO child based on external body dimensions reported by Snyder et al. (1977) [16], in which the mean stature was 1.377±0.063 m and the mean weight was 33.1±6.6 kg. In Phase Two, additional sets of image data from 94 subjects (5-29 subjects per body region) were used to verify and adjust the dimensions of skeletal components. The selected subjects were with an average stature of 1.403±0.091 m and an average weight of 37.6±9.9 kg. Surface contours of major body parts were created using a commercially available image processing software, Mimics (v. 10) (Materialise, Leuven, Belgium) and assembled to form the whole-body CAD model. Some structures, such as ligaments were based on the sites of insertion and origin described in anatomy resources [17, 18] because clinical images lacked the needed clarities. Detailed descriptions of the CAD modeling was documented in [19]. The stature and weight for the current CHARM-10 (standing) is 1401 mm and 35.0 kg, respectively.

In the process of meshing, the CAD model was further converted to mesh elements. ANSYS ICEM CFD (v. 12.1) (ANSYS, Canonsburg, PA) was used to generate hexahedral meshes based on a multi-block meshing scheme. This scheme is aimed at producing hexahedral elements in three-dimensional (3D) space, based on rules for geometrical grid-subdivisions (i.e. blocks) and mapping techniques [20]. Using this approach, the mesh size can be changed by altering the parameters of blocks while the shape remaining unchanged. Some complex cavities with soft tissues were enclosed and filled with tetrahedral elements, using the tetra-meshing tool in HyperMesh (v. 10.0) (Altair, Troy, MI). LS-DYNA (v.971) (LSTC, Livermore, CA) was used for FE simulations and analyses.

The main development task was divided into three parallel subtasks, i.e. the sub-models of head-neck, thorax-upper extremities (torso) and pelvis-lower extremities (PLEX) were developed in parallel. The general criteria used to determine the overall mesh qualities are as follows: Jacobian value larger than 0.3, aspect ratio less than 5.0, warpage less than 50° and skew less than 60°.

Material model and properties

The material properties of each body component were taken from open literature and documented in [11-15]. The material models and their parametric values are briefly summarized in Table 1.

TABLE 1

SUMMARY OF MATERIAL MODEL AND PARAMETERS

Part	Material model	Element property	Material parameters	Reference	CHARM-10 paper
Cortical: Cervical Spine	Elastic-plastic with power law	Shell, t=0.265 mm	E=13.44 GPa, k=355 MPa, N=0.277	[21]	[11]
Cortical: Rib, Sternum	Elastic-plastic	Shell, t=0.57 mm	E=6.48 GPa; σ_Y=64.6 MPa	Range from literatures	[14]
Cortical: Pelvis	Elastic-plastic	Shell, t=1.6 mm	E=12.24 GPa; σ_Y=150 MPa	[22]	[15]
Cortical: lower limb Long bones	Elastic-plastic	Shell at epiphysis; solid at diaphysis	E: from 0.854 GPa (femoral head) to 14.9 (tibia shaft) GPa	[23, 24]	[15]
Trabecular: Cervical spine	Elastic-plastic with power law	Solid	E=241 MPa, k=5.73 MPa, N=0.274	[25]	[11]
Trabecular: Rib, Sternum	Elastic-plastic	Solid	E=252.4 MPa, σ_Y=3.52 MPa	Range from literatures	[14]
Trabecular: Pelvis	Elastic-plastic	Solid	E=44.8 MPa, σ_Y=7.5 MPa	[22]	[15]
Trabecular:	Elastic-plastic	Solid	E: 250 MPa (distal femur) to 770	[23, 24]	[15]

Lower limb long bones			MPa (femoral head)		
Cartilage: Facet	Elastic	Solid	E=10 MPa	[26]	[11]
Cartilage: Costal	Elastic	Solid	E=3.3 MPa	Range from literatures	[14]
Cartilage: Pubic symphysis	Hyperelastic	Solid	Mooney-Rivlin parameters: G=0.5MPa C_{10}=0.05 MPa, C_{01}=0.2 MPa, C_{11}=0.25 MPa	[27]	[15]
Growth plate: Cervical spine	Elastic	Solid	E=25 MPa	[28]	[11]
Vertebral Endplate	Elastic-plastic with power law	Shell, t=0.45mm	E=4.48 GPa; k=118 MPa, N=0.277	[25]	[11]
Intervertebral Nucleus	Fluid	Solid	K=1.72 GPa	[29]	[11]
Lung	Lung tissue	Solid	K=50 MPa, C=3.88×10^{7}, α=5.85, β=-3.21, $C1$=1.265×10^{-8}, $C2$=2.71	[30, 31]	[14]
Heart	Viscous-elastic	Solid	K=2.6 MPa, $G0$=0.44 MPa, $G\infty$=0.15 MPa		[14]
Skin	Elastic	Membrane, t=1mm	E=1.0 MPa	[32]	[15]
Ligaments at cervical spine	Non-linear	Bar	Loading curves applied	[33]	[11]
Ligaments at pelvis	Linear	Bar	Tensile constants applied	[34, 35]	[15]

Notes: t: thickness; E: Young's modulus; k: strength coefficient; N: hardening coefficient; σ_Y: yield stress; K: bulk modulus. The other parameters are material coefficients in unit system: kg-mm-ms.

Model Validations at component/body part level

After meshing all body parts, validations of aforementioned three sub-models were conducted and documented in [11-15]. Table 2 summarizes these validations, including body part, loading condition, basic information of tested subjects and the references for the tests and model development/validation studies. If direct validation against pediatric subjects was not capable, adult data were used with a certain scaling laws.

TABLE 2

SUMMARY OF THE VALIDATIONS AT COMPONENT OR BODY PART LEVEL

Sub-model	Body part	Loading condition	Subjects tested	References for tests	References for CHARM-10
Head-neck	Head	Frontal impact	Adult PMHS	[36]	Appendix A
	Neck (segments)	Tension, flexion and extension	Pediatric PMHS Adult PMHS (scaled)	[37-39]; [40]	[11]
	Neck (whole cervical spine)	Tension, flexion and extension	Pediatric PMHS	[38, 41]	[11]
	Neck (whole cervical	Low-speed sled test	Pediatric volunteer	[42, 43]	[12]

	spine)				
Torso	Thorax	CPR (Anterior posterior compression)	Pediatric patients	[44]	[14]
	Thorax	Belt loading	Pediatric PMHS	[45, 46]	[13]
	Abdomen	Belt loading	Pediatric PMHS	[45, 46]	Appendix B
	Thorax	Frontal pendulum impact	Pediatric PMHS	[47]	[13]
PLEX	Pelvis	Lateral plate impact	Pediatric PMHS	[48]	[15]
	Pelvic girdle	Lateral impact to acetabulum	Adult PMHS (Results scaled)	[49]	[15]
	Femur, Tibia, Fibula	3-point bending	Pediatric PMHS	[50]	[15]
	Thigh, leg	3-point bending (dynamic)	Adult PMHS (Results scaled)	[51]	[15]
	Knee	4-pointbending (dynamic)	Adult PMHS (Results scaled)	[52]	[15]

Whole-body model integration

At the integration stage, the three developed and validated sub-models: head-neck, torso (thorax-upper extremities) and PLEX (pelvis-lower extremities) were integrated into a whole-body model, as shown in Fig. 2 (a).

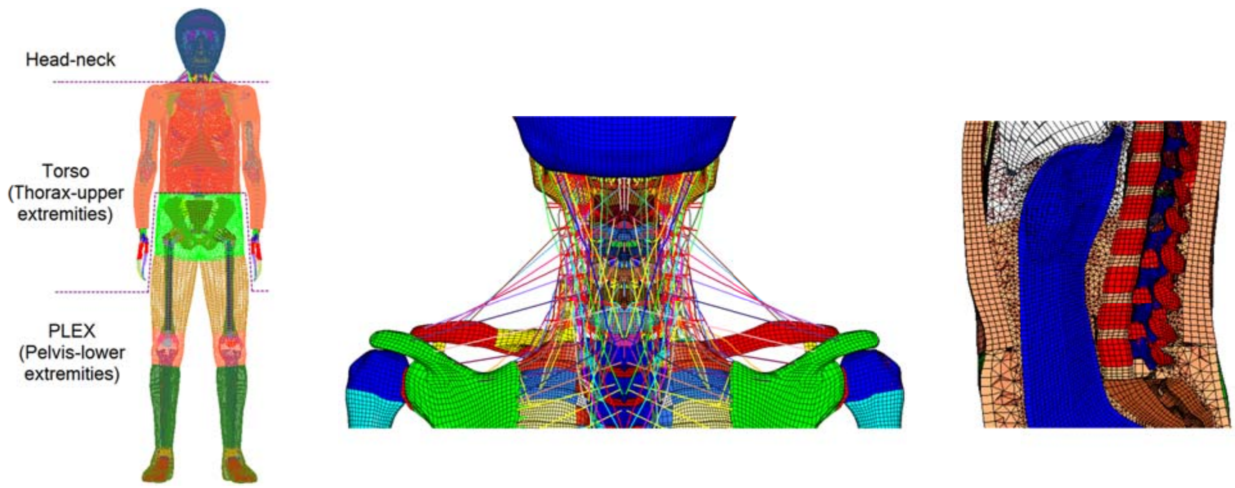

(a) (b) (c)

Fig. 2: Model integration. (a) Division of three sub-models developed in parallel; (b) muscle re-connection during head-neck and torso sub-models integration (rear view); (c) internal gaps merging and re-meshing (in tetrahedral elements) during torso and PLEX sub-models integration (a para-sagittal view)

All previous meshed parts were in the same anatomical positions (at standing posture) for assembling. The strategies of integration for different body regions are described as follows: (1) For the surface through the boundary, a strip of trilateral elements was built to connect the edges with different numbers of nodes. (2) For the connection of attaching 3D parts with different mesh densities, the LS-DYNA keyword CONTACT_TIED was used. For example, the inferior surface of the intervertebral disc between C7 and T1 vertebrae, which was part of the head-neck sub-model, was tied to the superior surface of T1 superior endplate. (3) For 1D ligament/muscle elements connecting across two sub-models, the reference nodes temporarily used for validations of sub-models were replaced with structural nodes located at identical geometric locations. The reconnection of muscles at the neck region is shown in Fig. 2 (b) as an illustration. (4) All major viscera (heart, lungs, kidneys, stomach, etc.) were individually modeled and hence there were gaps among them. Tetrahedral elements were used to fill these gaps during the sub-modeling process. In the integration of two adjacent sub-models, the gap filling tetra-meshes in each sub-model were deleted and then the newly formed space was refilled with new tetrahedral elements. Fig. 2 (c) showed an example at abdomen region. The general information of this whole-body FE model representing a 10 YO child is listed in Table 3.

TABLE 3
CHARM-10 OVERVIEW (STANDING POSTURE)

Number of parts	Number of nodes	Number of elements	Number of contacts (including node-to-part constrains)	Hexahedral vs. Tetrahedral	Quadrilateral vs. triangle	Original time step size
993	949,311	1,678,610	212	98.3% vs. 1.7%*	93.5% vs. 6.5%	6.2×10^{-5}ms

Jacobian < 0.3	Aspect ratio > 5.0	Warpage > 50.0°	Skew > 60.0°
2D: 0%	2D: 0.07%	2D: <0.01%	2D: 0.03%
3D: <0.01%	3D: 0.15%	3D: <0.01%	3D: 0.83%

*: The tetrahedral elements at joints regions and internal fat tissue among viscera and inner wall of fleshes were excluded.

III. WHOLE-BODY MODEL PRELIMINARY VALIDATIONS

Whole-body pedestrian impact

Since PHMS study was rarely available in literature, a typical car-to-pedestrian lateral impact scenario was created and FE simulations were carried out and compared with the other simulation using multi-body model. A detailed small sedan FE model, published on Dec. 21, 2011 was obtained from the National Crash Analysis Center (NCAC) website. The model was then simplified and only the front portion including the front bumper and hood, etc. was used to save computational time. A constant speed of 10 m/s (36 km/h) was assigned to the simplified car model that hit the CHARM-10 (standing) in lateral direction.

MADYMO (v.7.5) (TASS, Helmond, Netherlands) was used for multi-body model development and impact simulation. The 50th percentile MADYMO ellipsoid pedestrian model (v. 5.0) was taken as the baseline model. MADYMO/Scaler, based on GEBOD population [53], was used to scale the MADYMO baseline model to a 10 YO multi-body model with the same height and weight of the CHARM-10 (1401 mm and 35.0 kg). Using coupling FE-multi-body version of MADYMO, the same car FE model, initial positioning and impact speed used in CHARM-10 pedestrian impact simulation were adapted in the simulation using 10 YO MADYMO scaled model. The kinematic results are shown in Table 4.

The comparison shows that, the CHARM-10 has similar kinematics histories as the 10 YO MADYMO model, especially on the upper body. However, the lower limbs of CHARM-10 exhibit more extents of motion off the bumper from 60 ms. Because the head-to-hood impact is the major cause of fatal head/brain injury, the relative motion of the head to hood is also analyzed. The initial head contact of CHARM-10 simulation occurs at 85 ms, while it is 84 ms in the 10 YO MADYMO simulation. The peak velocities of the head center of gravity (CG) in vertical direction are 7.8 m/s and 8.0 m/s, for the FE and multi-body models respectively. The comparison demonstrates that the kinematic responses of the CHARM-10 (standing) are close to those of multi-body model, especially in terms of upper body and head motion.

It should be noted that the 10 YO MADYMO model was generated by scaling an adult pedestrian model to a 10

YO child, which was not validated. Subsequently, the simulation study should be considered as a robustness check and kinematic corroboration, rather than a complete validation.

TABLE 4

PEDESTRIAN LATERAL IMPACT SIMULATION RESULT COMPARISON

Model	0 ms	20 ms	40 ms
10 YO FE pedestrian model			
10 YO MADYMO model (Scaled from adult model)			
Model	**60 ms**	**80 ms**	**100 ms**
10 YO FE pedestrian model			
10 YO MADYMO model (Scaled from adult model)			

Model posture change

In order to simulate occupant responses, the standing posture model was converted to a seated posture. This was accomplished by joint rotations and spine repositioning. Firstly, the tetra meshes and ligaments around the hip, knee, and ankle joints were removed. Skeletal rotations about the center of femoral head, lateral femoral condyle, and lateral malleolus were then carried out in sequence at these three joints. After the rotation, the ligaments at these joints were rebuilt according to the normal physiological state in a seated position [17, 18]. The outer skin at a joint was morphed along with the rotation using HyperMopher tool of HyperMesh. The inner surface of the surrounding flesh/fat was also changed. Using the adjusted outer skin and inner surface at the joint region, a new enclosed space was achieved so that tetrahedral elements for flesh/fat at the joints could be re-generated.

For sled test simulations, the spine was repositioned to follow the curvature described in [54]. The positioning process was done by applying prescribed motions to the head, C4, T1, T4 and T8. The final geometry was exported as the initial condition for the sled test simulations. As shown in Fig. 3, little discrepancies were found between the model and average posture of volunteers tested.

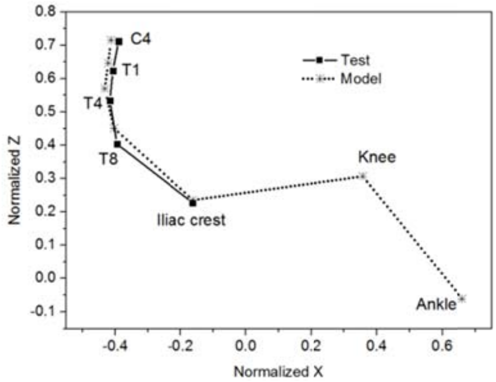

Fig. 3: Model posture change result, compared with the average posture of seated volunteer in [54].

During the posture change, the mesh quality was carefully controlled. After this phase, the mesh quality of CHARM-10 seated posture was re-assessed using the same criteria listed in Table 3. A total of 0.85% of 3D elements failed for skew angle criterion. For all other criteria such as Jacobian, warpage angle and aspect ratio, the percentages of elements with lower quality were 0.2% or less. The original time step stays unchanged.

Whole-body occupant sled test

The seated model was used to predict the responses in two loading conditions which were designed to simulate frontal car crashes, namely (1) low-speed sled test on child volunteers [54] and (2) high-speed sled test on a child PMHS [55]. The information regarding subjects tested and loading conditions are summarized in Table 5.

TABLE 5

INFORMATION OF THE SUBJECTS, LOADING CONDITIONS AND BELT FORCE OUTPUTS OF SLED TESTS (±STANDARD DEVIATION)

Reference	Subject	Age (year)	Stature (mm)	Weight (kg)	Impact velocity (m/s)	Peak deceleration (g)	Duration of deceleration (ms)
Arbogast et al. 2009 [54]	6 volunteers	10.2 ±0.8	1378 ±92	32.3 ±5.3	2.32±0.14	3.62±0.29	~125
Ash et al. 2009 [55]	1 PMHS	13	1390	31	11.4	~22	~70

In both scenarios, the subject was positioned on a seat and restrained by a three-point belt. The seat was mounted on a crash sled, which was decelerated by a hydraulic system (pulse generator). Markers were placed on selected body locations such as the ear, acromion, iliac crest and knee to trace the kinematic response in the sagittal plane. The experimental setup and subject postures of the two tests are shown in Fig. 4 (a) and (b), respectively. It should be noted that the PMHS in the high-speed test was a 13 YO, and the belt forces and trajectories were scaled to 10 YO and reported by the investigators in [55].

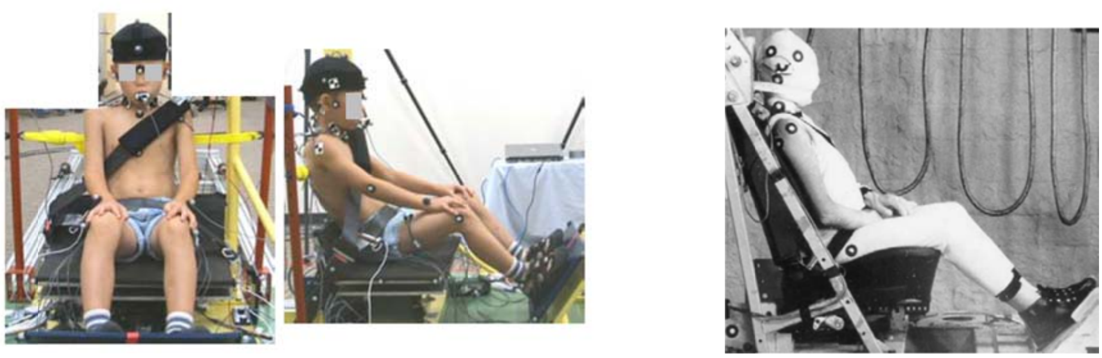

(a) (b)

Fig. 4: Experimental setup and subject posture of the sled tests: (a) low-speed sled test on child volunteers (adapted from [54]) and (b) high-speed sled test on a 13 YO PMHS (adapted from [55])

In simulations of sled tests, the CHARM-10 (seated) model was placed on a simplified seat and restrained with a three-point seat belt model. The setup of the numerical model for the low-speed sled test is shown in Fig. 5. The seat used in [54] had an aluminum horizontal seat pan (495 mm x 305 mm) with a low-back supporter (127 mm high and 18° reclined from vertical). The polyurethane padding was 6.5 mm thick. In numerical simulation, the seat pan and back support were modeled as rigid plates. No initial gravity-induced equilibrium condition was conducted because an earlier parametric study (using the rigid seat model) suggested no significant difference between the models with and without pre-impact equilibrium setting.

In Arbogast experiments, an automatic locking retractor was used. In the simulation, the retractor was simulated using LS_DYNA keyword ELEMENT_SEATBELT_RETRACTOR and its activation timing was based on belt force history reported in [54]. The keyword ELEMENT_SEATBELT_SLIPRING was used to model the upper and lower anchors. The shoulder belt centerline was set to pass over the clavicle and sternum, while the lap belt centerline engaged the two iliac wings, as described in [54]. The BeltFit tool in LS-PrePost was utilized to generate the 2D elements of the belts, so that the belts contact the outer skins smoothly.

Muscles in the neck region were represented by the Hill type muscle model (available in LS-DYNA as material type No. 156) to simulate the passive and active responses. Dong et al. [12] utilized a set of optimization procedures to identify the activation level, initial time and end time of neural excitation to best match the head rotation time histories predicted by the FE model and measured in volunteer tests in [54]. The same properties used in [12] were adopted in the current study for low-speed sled test simulation. In the simulation of the high-speed PMHS test, active functions of muscles were deactivated while the passive function remains intact.

The same model posture used in low-speed simulation was assumed for the high-speed simulation, since no posture details of PMHS were available in [55]. The setup of the high-speed sled test was close to that of low-speed sled test, except changes of seat and belt configurations. The deceleration pulse for the low-speed test was extracted and modified from bumper car impact, while the pulse for the high-speed test was trapezoidal from a 41 km/h sled impact. The deceleration pulses were applied in the numeric simulations, shown in Fig. 6.

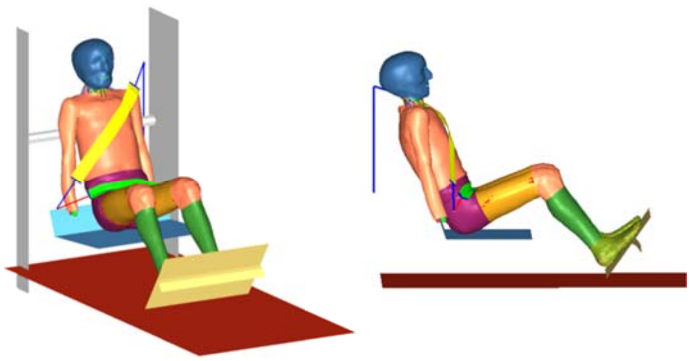

Fig. 5: Simulation setup for low-speed sled test

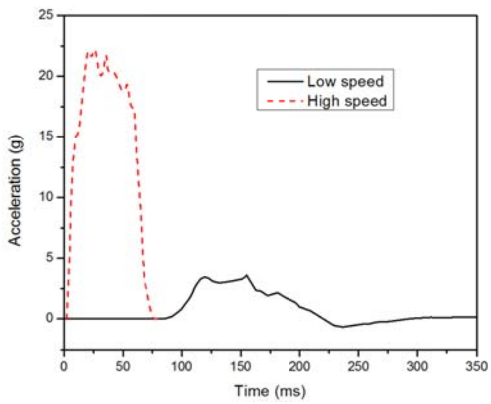

Fig. 6: Deceleration pulses applied in the simulations

The model-predicted belt forces, including the shoulder and lap belt force-time histories were compared with the measurements obtained in the tests, as shown in Fig. 7. The model-predicted peak lap belt force was 243 N in the low-speed case, compared reasonably well with the test result (average 277 N, ranged 40 to 610 N). However, the peak shoulder belt force was 453 N, which was 38% higher than the average test result (329 N) but still within the range reported in the tests (140 to 530 N). Additionally, the time to peak of shoulder belt force from simulation was 23 ms shorter than the reported test average.

In high-speed sled test simulation, the predicted peak lap belt force was 3765 N, which was 8.6% lower than that measured experimentally. The peak shoulder belt force predicted by the model was 4962 N, which was 20.0% higher than the test result.

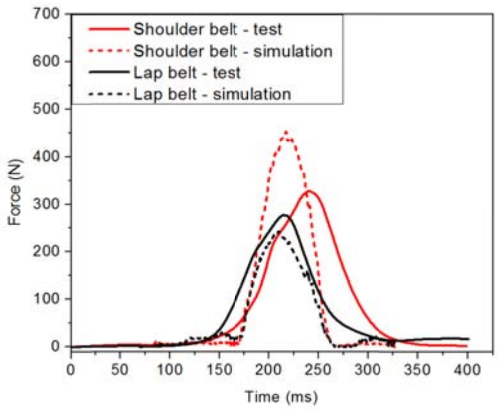

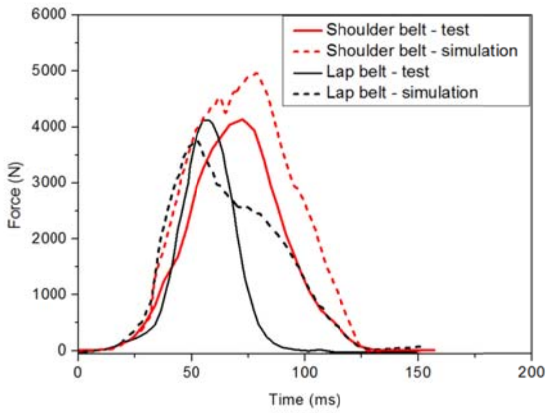

(a) (b)

Fig. 7: Comparison of the belt forces predicted by the FE model and measured by tests. (a) low-speed case, (b) high-speed case

For the low-speed experimental studies, the reported excursions were based on a normalization procedure done by dividing the marker coordinates by the seated height. The same normalization method was applied to the model-predicted results and comparisons plotted in Fig. 8 (a). For the high-speed experiment, Ash et al. reported the trajectories by scaling the experimental data to a 10 YO [55]. Direct comparison of the model-predicted excursions was made and shown in Fig. 8 (b). It was found that the trajectories predicted by the CHARM-10 (seated) model reasonably match the kinematic results in both low-speed and high-speed tests.

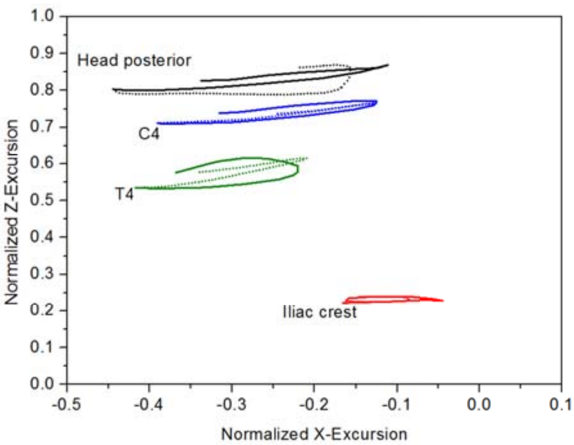

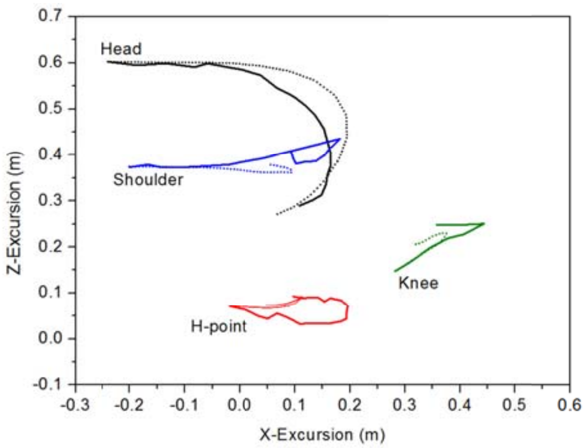

(a) (b)

Fig.8: Comparison of the trajectories: (a) low-speed case (normalized) and (b) high-speed case (scaled data by Ash et al). Solid curves: test results; dashed curves: simulation results; X- and Z-excursions are defined as the excursion at the posterior-anterior and inferior to superior direction, respectively.

IV. DISCUSSION

Limitations of the whole-body model validations

Injury related validations done at component level were reported in previous papers as listed in Table 2. For example, the 3-point bending induced fracture in the leg, tensile ruptures in the neck ligaments, etc. The current study did not include injury prediction because of the paucity of pediatric whole-body test data in intense loading conditions. Given the fact that reasonable biomechanical responses under various loading conditions were predicted by the whole-body model, there is a good potential that it can be applied for predicting injuries. Future works should consider collecting fall or traffic accident induced injuries to check the potential of using

CHARM-10 to predict real world injury. More limitations of each corroboration/validation are stated as follows.

CHARM-10 (standing) model was corroborated by comparing the kinematics to that calculated by the reference 10 YO MADYMO model developed using a scaling method. Despite the fact that two models were in good agreement, none of them can be considered validated. At best, the similarities found between two different models using two different software packages suggest that the kinematic response predicted by CHARM-10 (standing) model subjected to lateral impact is reasonable.

For CHARM-10 (seated) low-speed sled test simulation, the initial positioning, muscle force, and belt model selected in the whole-body sled test simulation all contributed to the variation observed in the shoulder belt force in terms of magnitude and timing. No attempt was made to correct the differences in part because of the lack of sufficient details listed in the experimental study. Additionally, the model-predicted peak shoulder force (453 N) was still within the measured peak shoulder force ranged from 140 to 530 N. No explanations were provided regarding this large discrepancy in the range obtained experimentally and it would be premature attempting to correct this difference.

In the high-speed sled test simulation, the tested subject was a 13 YO with larger anthropometric dimensions than an average 10 YO child. Although scaled data were reported in the PMHS study paper, details of the seat, seat belts and precise spinal curvature were not available. For these reasons, some errors may be added to the simulation.

Future work

For the finished component and sub-model level validations summarized in Table 2, the loading for lower body validation are mainly at lateral direction, while those for the torso are mainly at fore-aft direction. In future, the CHARM-10 model should be further validated in more loading conditions. More test data from adults can potentially be used for model improvement, with careful selection or development of specific scaling laws. Accident reconstruction is another possible approach to improve the model's capability of injury prediction.

Epiphyseal growth plate is another point of interest. As summarized in [56], earlier epidemiological studies revealed that 15-20% of all childhood fractures were growth plate related. These structures typically lie at the ends of long bones of skeletally immature humans. The mechanical weakening may have significant effect on the biomechanical responses according to a parametric study [15]. Most growth plates are not modeled in the current version of CHARM-10. This is in part due to the fact that biomechanical properties of growth plate are largely unknown and growth plate injury was not routinely reported in accident database. When human test data involving growth plates become available, detailed models consist of growth plates could be developed to achieve a higher biofidelity.

V. CONCLUSIONS

To facilitate the investigation of pediatric injury mechanism and advanced protection techniques, efforts were devoted to the development of a whole-body FE model of an average 10 YO child (CHARM-10) with sufficient details. The integration of three sub-models of the head-neck, torso and PLEX was successfully conducted. Full body simulations were performed at both standing and seated postures. The simulation results using the CHARM-10 (standing) have a reasonable agreement with a multi-body simulation under the same impact condition, in terms of motion history and head impact timing and velocity. The simulations of low-speed and high-speed sled tests using the CHARM-10 (seated) were compared to the experimental data of volunteers and a PHMS, respectively. The belt force histories and body motions predicted by the FE model showed a satisfactory match with the test data, except a higher shoulder belt force found in low-speed simulation. To conclude, the pediatric pedestrian and occupant models for 10 YO children (CHARM-10 standing and seated) are numerically stable, kinematically corroborated against car-to-pedestrian multi-body simulation, and preliminarily validated against occupant frontal impact. It should be noted that the CHARM-10 model at this stage should not be treated as fully validated, since the validations are still incomplete due to lack of pediatric data. Further model improvement is needed before applications in automotive safety research.

VI. ACKNOWLEDGEMENT

This work was financially supported by Toyota's Collaborative Safety Research Center (MI, US), and partially supported by the National Science Foundation for Young Scientists of China (Grant number 51405148).

VII. REFERENCES

1. Arbogast, K B, Durbin D R. Epidemiology of child motor vehicle crash injuries and fatalities, *Pediatric Injury Biomechanics*. 2013, *Springer*: 33-86.
2. WHO. World report on child injury prevention. 2008.
3. Wazana, A, Krueger P, Raina P, Chambers L. A review of risk factors for child pedestrian injuries: are they modifiable? *Injury Prevention*, 1997, 3 (4): 295-304.
4. NHTSA. Traffic Safety Facts 2012 data - Pedestrian. *Government Report*, 2014 (DOT HS 811 888).
5. Jarrett, K, Saul R. Pedestrian injury-analysis of the PCDS field collision data. *Proceedings of the 16th International Technical Conference on the Enhanced Safety of Vehicles (ESV),* 1998, Windsor, Ontario, CA.
6. NHTSA. Traffic Safety Facts 2011 data - Children. *Government Report*, 2013 (DOT HS 811 767).
7. Mizuno, K, Iwata K, Deguchi T, Ikami T, Kubota M. Development of a three-year-old child FE model*. Traffic Injury Prevention*, 2005, 6 (4): 361-371.
8. Okamoto, M, Takahashi Y, et al. Development of finite element model for child pedestrian protection. *Proceedings of the 18th International Technical Conference on the Enhanced Safety of Vehicles (ESV),* 2003, Nagoya, Japan.
9. Ito, O, Okamoto M, Takahashi Y, Mori F. Validation of an FE Lower Limb Model for a Child Pedestrian by Means of Accident Reconstruction*. SAE International Journal of Passenger Cars-Mechanical Systems*, 2009, 1 (1): 971-984.
10. Kim, J E, Li Z, et al. Finite element model development of a child pelvis with optimization-based material identification*. Journal of Biomechanics*, 2009, 42 (13): 2191-2195.
11. Dong, L, Li G, Mao H, Marek S, Yang K H. Development and validation of a 10-year-old child ligamentous cervical spine finite element model*. Annals of Biomedical Engineering*, 2013, 41 (12): 2538-2552.
12. Dong, L, Mao H, Li G, Yang K H. Investigation of pediatric neck response and muscle activation in low-speed frontal impacts. *Computer methods in biomechanics and biomedical engineering*, 2015 (In press).
13. Jiang, B, Mao H, Cao L, Yang K H. Experimental Validation of Pediatric Thorax Finite Element Model Under Dynamic Loading Condition and Analysis of Injury. *SAE Technical Paper*, 2013 (No. 2013-01-0456).
14. Jiang, B, Cao L, et al. Development of a 10-year-old paediatric thorax finite element model validated against cardiopulmonary resuscitation data*. Computer methods in biomechanics and biomedical engineering*, 2014, 17 (11): 1185-1197.
15. Shen, M, Zhu F, et al. Finite element modeling of 10-year-old child pelvis & lower extremities with growth plates for pedestrian protection. *International Journal of Vehicle Safety*, 2015 (In press).
16. Snyder, R, Schneider L, et al. Anthropometry of Infants, Children, and Youths to Age 18 for Product Safety Design. Final Report. *Consumer Product Safety Commission Report*, 1977 (No. UM-HSRI-77-17).
17. Gray, H. Gray's Anatomy of Human Body. 1918 (Accessed: 2013 Nov. 1st); Available from: https://education.yahoo.com/reference/gray/subjects/subject/57.
18. Moore, K L, Agur A M R, Dalley A F. Essential clinical anatomy. 4th ed. 2011, *Lippincott Williams & Wilkins*: Baltimore, MD.
19. Mao, H, Holcombe S, et al. Development of a 10-Year-Old Full Body Geometric Dataset for Computational Modeling*. Annals of Biomedical Engineering*, 2014, 42 (10): 2143-2155.
20. Shivanna, K H, Tadepalli S C, Grosland N M. Feature-based multiblock finite element mesh generation*. Computer-Aided Design*, 2010, 42 (12): 1108-1116.
21. Currey, J D. Tensile yield in compact bone is determined by strain, post-yield behaviour by mineral content*. Journal of Biomechanics*, 2004, 37 (4): 549-556.
22. Kim, J E, Hsieh M H, Soni B K, Zayzafoon M, Allison D B. Childhood Obesity as a Risk Factor for Bone Fracture: A mechanistic study*. Obesity*, 2013, 21 (7): 1459-1466.
23. Takahashi, Y, Kikuchi Y, Konosu A, Ishikawa H. Development and validation of the finite element model for the human lower limb of pedestrians*. Stapp Car Crash Journal*, 2000, 44 (1): 335-355.
24. Untaroiu, C, Darvish K, Crandall J, Deng B, Wang J T. A finite element model of the lower limb for simulating

pedestrian impacts. *Stapp Car Crash Journal*, 2005, 49 (1): 157-181.

25. Kopperdahl, D L, Keaveny T M. Yield strain behavior of trabecular bone. *Journal of Biomechanics*, 1998, 31 (7): 601-608.
26. Yamada, H, Evans F G. Strength of biological materials. 1970, *Williams & Wilkins*: Baltimore.
27. Li, Z, Alonso J E, et al. Three-dimensional finite element models of the human pubic symphysis with viscohyperelastic soft tissues. *Annals of Biomedical Engineering*, 2006, 34 (9): 1452-1462.
28. Cohen, B, Chorney G S, et al. The microstructural tensile properties and biochemical composition of the bovine distal femoral growth plate. *Journal of Orthopaedic Research*, 1992, 10 (2): 263-275.
29. Yang, K H, Zhu F, Luan F, Zhao L, Begeman P C. Development of a finite element model of the human neck. *Stapp Car Crash Journal*, 1998, 42: 195-205.
30. Shah, C S, Yang K H, Hardy W, Wang H K, King A I. Development of a computer model to predict aortic rupture due to impact loading. *Stapp Car Crash Journal*, 2001, 45: 161-182.
31. Ito, O, Dokko Y, Ohashi K. Development of Adult and Elderly FE Thorax Skeletal Models. *SAE Technical Paper*, 2009 (No. 2009-01-0381).
32. Yue, N, Shin J, Untaroiu C D. Development and validation of an occupant lower limb Finite element model. *SAE Technical Paper*, 2011 (No. 2011-01-1128).
33. Chazal, J, Tanguy A, et al. Biomechanical properties of spinal ligaments and a histological study of the supraspinal ligament in traction. *Journal of Biomechanics*, 1985, 18 (3): 167-176.
34. Hewitt, J, Guilak F, Glisson R, Vail T P. Regional material properties of the human hip joint capsule ligaments. *Journal of Orthopaedic Research*, 2001, 19 (3): 359-364.
35. Bechtel, R. Physical characteristics of the axial interosseous ligament of the human sacroiliac joint. *The Spine Journal*, 2001, 1 (4): 255-259.
36. Nahum, A M, Smith R, Ward C C. Intracranial pressure dynamics during head impact. *SAE Technical Paper*, 1977 (No. 770922).
37. Luck, J F, Nightingale R W, et al. Tensile mechanical properties of the perinatal and pediatric PMHS osteoligamentous cervical spine. *Stapp Car Crash Journal*, 2008, 52: 107-134.
38. Luck, J F. The biomechanics of the perinatal, neonatal and pediatric cervical spine: investigation. 2012, *PhD Dissertation*, *Duke University*.
39. Luck, J F, Nightingale R W, et al. Tensile failure properties of the perinatal, neonatal, and pediatric cadaveric cervical spine. *Spine*, 2013, 38 (1): E1-E12.
40. Nightingale, R W, Chancey V C, et al. Flexion and extension structural properties and strengths for male cervical spine segments. *Journal of Biomechanics*, 2007, 40 (3): 535-542.
41. Ouyang, J, Zhu Q, et al. Biomechanical assessment of the pediatric cervical spine under bending and tensile loading. *Spine*, 2005, 30 (24): E716-E723.
42. Dibb, A T. Pediatric head and neck dynamic response: A computational study. 2011, *PhD Dissertation*, *Duke University*.
43. Panzer, M B, Fice J B, Cronin D S. Cervical spine response in frontal crash. *Medical Engineering & Physics*, 2011, 33 (9): 1147-1159.
44. Maltese, M R, Castner T, et al. Methods for determining pediatric thoracic force-deflection characteristics from cardiopulmonary resuscitation. *Stapp Car Crash Journal*, 2008, 52: 83-105.
45. Kent, R, Lopez-Valdes F J, et al. Characterization of the pediatric chest and abdomen using three post-mortem human subjects. *Proceedings of the 22nd International Technical Conference on the Enhanced Safety of Vehicles (ESV),* 2011, Washington, DC, US.
46. Kent, R, Salzar R, et al. Pediatric thoracoabdominal biomechanics. *Stapp Car Crash Journal*, 2009, 53: 373-401.
47. Ouyang, J, Zhao W, Xu Y, Chen W, Zhong S. Thoracic impact testing of pediatric cadaveric subjects. *Journal of Trauma and Acute Care Surgery*, 2006, 61 (6): 1492-1500.
48. Ouyang, J, Zhu Q, et al. Experimental cadaveric study of lateral impact of the pelvis in children. *Academic Journal*

of the First Medical College of PLA, 2003, 23 (5): 397-401, 408.

49. Guillemot, H, Besnault B, et al. Pelvis Injuries in Side Impact Collisions : A Field Accident Analysis and Dynamic Tests on Isolated Pelvis Bones. *SAE Technical Paper*, 1997 (No. 973322).

50. Ouyang, J, Zhu Q, Zhao W. Biomechanical character of extremity long bones in children and its significance. *Chinese Journal of Clinical Anatomy*, 2003, 21 (6): 620-623.

51. Kerrigan, J R, Drinkwater D C, et al. Tolerance of the human leg and thigh in dynamic latero-medial bending. *International Journal of Crashworthiness*, 2004, 9 (6): 607-623.

52. Bose, D, Bhalla K, et al. Response of the Knee Joint to the Pedestrian Impact Loading Environment. *SAE Technical Paper*, 2004 (No. 2004-01-1608).

53. TASS International. MADYMO Utilities Manual Release 7.2. 2010, *https://www.tassinternational.com/software-support*.

54. Arbogast, K B, Balasubramanian S, et al. Comparison of kinematic responses of the head and spine for children and adults in low-speed frontal sled tests. *Stapp Car Crash Journal*, 2009, 53: 329-372.

55. Ash, J, Sherwood C, et al. Comparison of anthropomorphic test dummies with a pediatric cadaver restrained by a three-point belt in frontal sled tests. *Proceedings of the 21st International Technical Conference on the Enhanced Safety of Vehicles (ESV),* 2009, Stuttgart, Germany.

56. Peterson, H A. Epiphyseal growth plate fractures. 2007, *Springer*: Heidelberg.

VIII. APPENDIX A: HEAD VALIDATION

The head model was loaded as the conditions of PMHS test No. 37 in Nahum's study [36]. The cylinder (mass: 5.59 kg) was hitting the front of skull at a speed of 9.94 m/s, with an angle of 45° (to the horizontal plane), as shown in Fig. 9 (a). The linear acceleration, as shown in Fig. 9 (b), was taken as the prescribed motion input to the head and brain model. The results of intracranial pressure (ICP) at coup and contrecoup positions were compared with the adult results in Fig. 10. No available scaling law was applied for quantitative comparison.

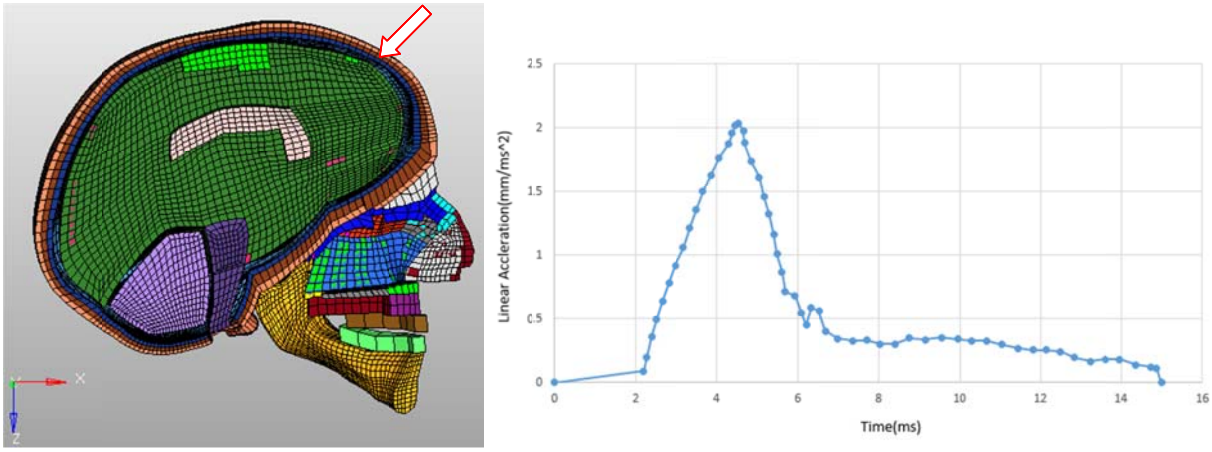

(a) (b)

Fig. 9: Simulation of the frontal impact of head: (a) Location of impact and scheme; (b) Acceleration – time history used to simulate the motion caused by impact

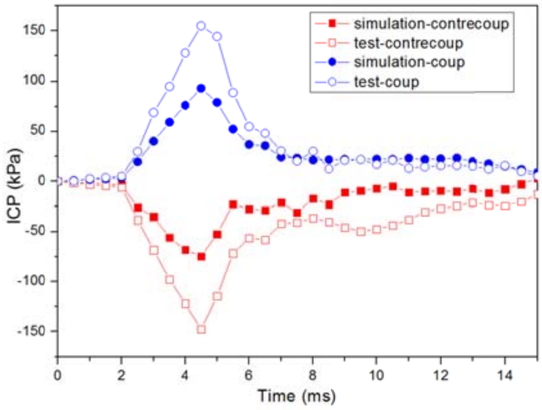

Fig. 10: Comparison of measured ICP in the adult brain and simulated ICP in the 10 YO brain

IX. APPENDIX B: ABDOMEN VALIDATION

The reference of PHMS tests were from Kent group [45, 46]. The dynamic loading cases were used for model validation, and reported belt displacement histories were taken as the loading inputs of the simulations. The peak displacement rates were approximate 1.6 m/s and 2.0 m/s for abdomen and chest, respectively. The loading configurations were shown in Fig. 11. Upper and lower abdomen was loaded by 5-cm-wide transverse belt and the chest was loaded by 16.6-cm-wide distributed belt. The diagonal belt loading simulation has been reported in [13] thus not included in this paper.

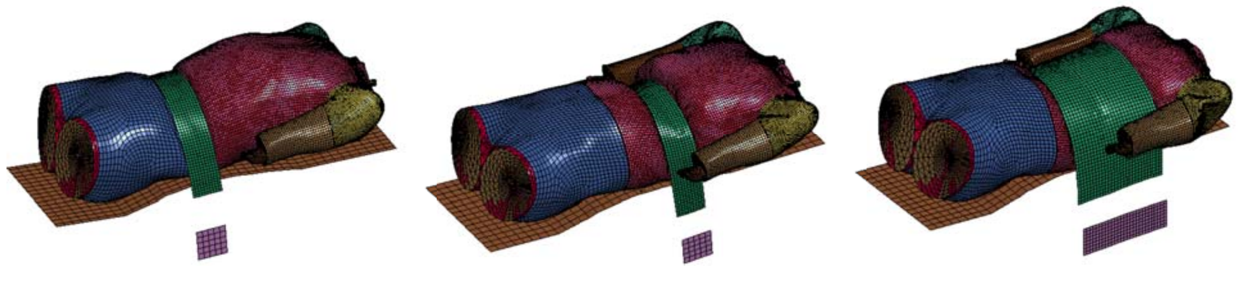

Fig. 11: Sketch of the belt loading with different configurations. (a) Lower abdomen loaded with transverse belt; (b) upper abdomen loaded with transverse belt; (c) upper abdomen - chest loaded with distributed belt

The reaction force of the posterior support plate in each case was recorded as the "Force." The mid-abdomen penetration for transverse belt cases and chest displacement (anterior-posterior) for distributed belt case were collected as the "Deflection", respectively. The Force-Deflection curves were plotted in Fig. 12, in comparison with the test data using pediatric PMHS. Reasonable agreements have been obtained in all three abdomen related loading cases.

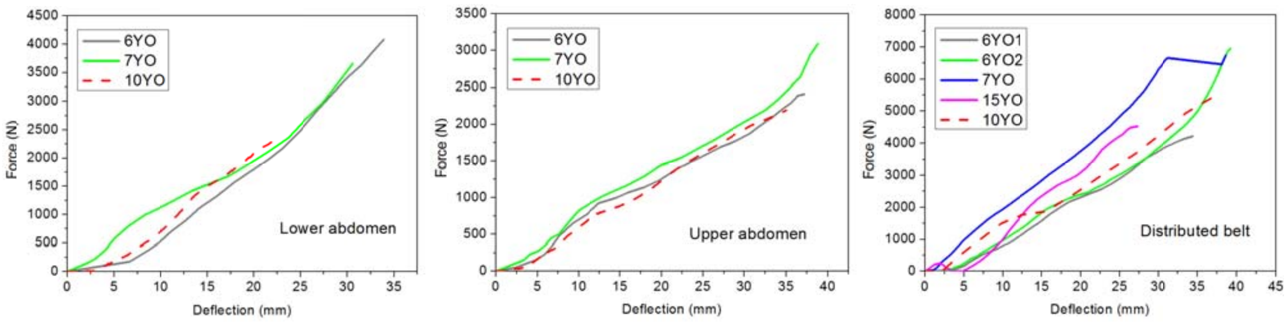

Fig. 12: Validation result of abdomen belt loading by comparing force-deflection curves predicted by the FE models and measured in pediatric PMHS tests (solid curves: test results; dashed curves: simulation results; PHMS ages are marked in legends)